

## Supplementary Information

### **Probing Lithium Germanide Phase Evolution and Structural Change in a Germanium-in-Carbon Nanotube Energy Storage System**

Wei Tang<sup>a,d</sup>, Yanpeng Liu<sup>a</sup>, Chengxin Peng<sup>a</sup>, Mary Y. Hu<sup>b</sup>, Xuchu Deng<sup>b</sup>, Ming Lin<sup>\*c</sup>,  
Jian Zhi Hu<sup>\*b</sup> and Kian Ping Loh<sup>\*a</sup>

<sup>a</sup>Department of Chemistry and Graphene Research Centre, National University of  
Singapore, 3 Science Drive 3, Singapore 117543

<sup>b</sup>Pacific Northwest National Laboratory, Richland, WA 99352, USA.

<sup>c</sup>Institute of Materials Research and Engineering, 3 Research Link, Singapore 117602.

<sup>d</sup>NUS Graduate School for Integrative Sciences and Engineering, 28 Medical Drive  
#05-01, Singapore 117597.

Corresponding author: Kian Ping Loh, Email: [chmlohkp@nus.edu.sg](mailto:chmlohkp@nus.edu.sg); Jian Zhi Hu,  
Email: [Jianzhi.Hu@pnnl.gov](mailto:Jianzhi.Hu@pnnl.gov); Ming Lin, Email: [m-lin@imre.a-star.edu.sg](mailto:m-lin@imre.a-star.edu.sg).

## Supplementary materials list

1. Growth process of Ge@CNT.
2. XRD monitoring of the precursors and products during sample preparation and Raman characterization.
3. Morphology of the catalyst Ge nanoparticles /MgO, bare Ge and Ge@CNT.
4. Electrochemical study of Ge@CNT and bare Ge
  - 4.1 Cyclic voltammograms (CVs) of Ge@CNT and bare Ge.
  - 4.2 Voltage profiles of Ge@CNT at 0.2C
  - 4.3 Rate capability of Ge@CNT and bare Ge
  - 4.4 Asymmetric rate study (fast-discharge and slow-charge) of Ge@CNT
  - 4.5 Cyclability and Voltage profiles of Ge@CNT.
  - 4.6 Ex-situ impedance study of Ge@CNT and bare Ge.
  - 4.7 Performance comparison of Ge@CNT and reported Ge-based anodes
5. TEM study of phase evolution using TEM-coin cell configuration
  - 5.1 Physical integrity of the Ge@CNT composite after being discharged to 0.17 V and charged to 0.5 V at 0.2C
  - 5.2 TEM images of Ge@CNT after 200cycles
6. In-situ NMR configuration
  - 6.1 The illustration of the NMR measurement cell
  - 6.2 In situ  $^7\text{Li}$  NMR spectra of the Ge@CNT composite
  - 6.3 Fitting method for NMR data
  - 6.4 Quantitative analysis of the phase compositions
7. Experimental details

## 1. Growth process of Ge@CNT.

As illustrated in Fig.S1, a Ge nanoparticle/magnesium oxide catalyst (Ge NP/MgO) was first prepared by ball-milling magnesium (Mg) and germanium dioxide ( $\text{GeO}_2$ ) together, during which a solid-state reduction of  $\text{GeO}_2$  resulted in the formation of Ge NPs coated with MgO (Fig.S1a). Supported on an alumina substrate, the composite was used to catalyse carbon nanotube (CNT) growth. To grow multiwall carbon nanotubes (MWCNTs), the catalyst was heated to 880 °C in a CVD furnace and a mixture of methane ( $\text{CH}_4$ ) and hydrogen ( $\text{H}_2$ ) gases was passed over it for 3 hours. To suppress growth of amorphous carbon, water vapour was introduced by bubbling part of the reaction gases through distilled water during the growth process<sup>1</sup>. As shown in Fig.S1b, during CVD, the Ge NPs were reshaped into nanorods (NRs) inside the CNTs and the NRs were coated with few- layer graphene uniformly. Following CVD, the Ge@CNT composite was collected by dissolving the MgO with hydrochloric acid (HCl) (Fig.S1c) and was characterised by XRD and Raman spectroscopy (Fig.S2, Fig.S3).

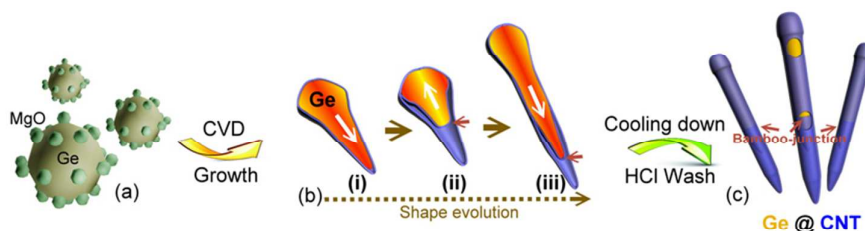


Fig.S1. Growth of the Ge@CNT composite using Ge NPs as seeds.

## 2. XRD monitoring of the precursors and products during sample preparation and Raman characterization.

Fig.S2 shows the XRD spectra of (1) Mg + GeO<sub>2</sub>, before ball milling and (2) after ball milling, where GeO<sub>2</sub> is successfully reduced into Ge, with some Mg<sub>2</sub>Ge impurity present. (3) After CVD growth, the crystallinity of Ge is improved (index in JCPDS card NO. 04-0545, diamond cubic Ge). (4) Finally, MgO is fully dissolved away from the composite using acid. Raman spectra of bare Ge and Ge@CNT are compared in Fig.S3. In the Raman spectra (Fig.S3), the peak located around 288 cm<sup>-1</sup> is due to the optical mode of crystalline Ge. Three peaks at 1336 cm<sup>-1</sup>, 1564 cm<sup>-1</sup> and 2672 cm<sup>-1</sup> are in good agreement with the typical Raman D, G and 2D bands of CNTs<sup>2</sup>, respectively. The D band of CNTs is often referred to as the disorder or defect mode. It is known that Li<sup>+</sup> can diffuse into Ge NRs through defects or disorder ‘gaps’ between graphitic sheets on CNTs<sup>2,3</sup>.

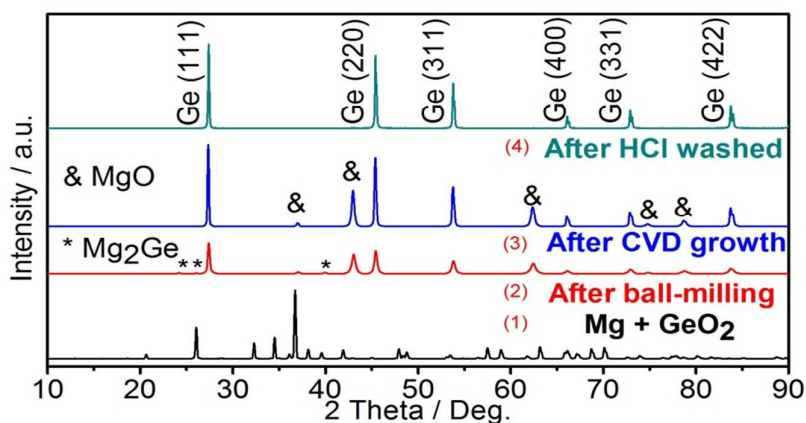


Fig.S2. Stacking XRD patterns monitoring the preparation process.

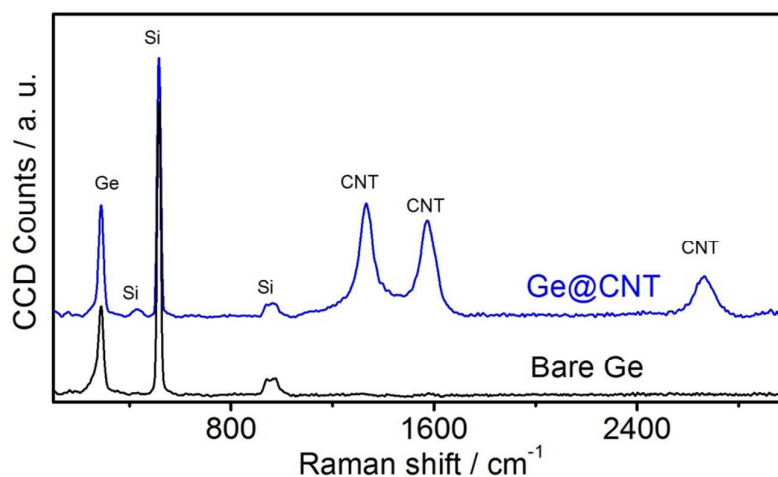


Fig.S3. Raman spectra of Ge@CNT and bare Ge.

### 3. Morphology of the catalyst Ge nanoparticles /MgO, bare Ge and Ge@CNT.

After ball-milling, the morphology of Ge NPs/MgO was characterized by TEM and STEM. Fig.S4a,b,c, show the typical TEM and STEM images of Ge NPs/MgO, which clearly indicate that Ge NPs are surrounded by small MgO clusters. After HCl washing, as shown in Fig.S4d,e, MgO clusters were washed away, leaving behind Ge NPs. Besides carrying out CVD growth to produce the Ge@CNT composites, these washed samples were also collected and marked as “bare Ge” for control experiments in batteries.

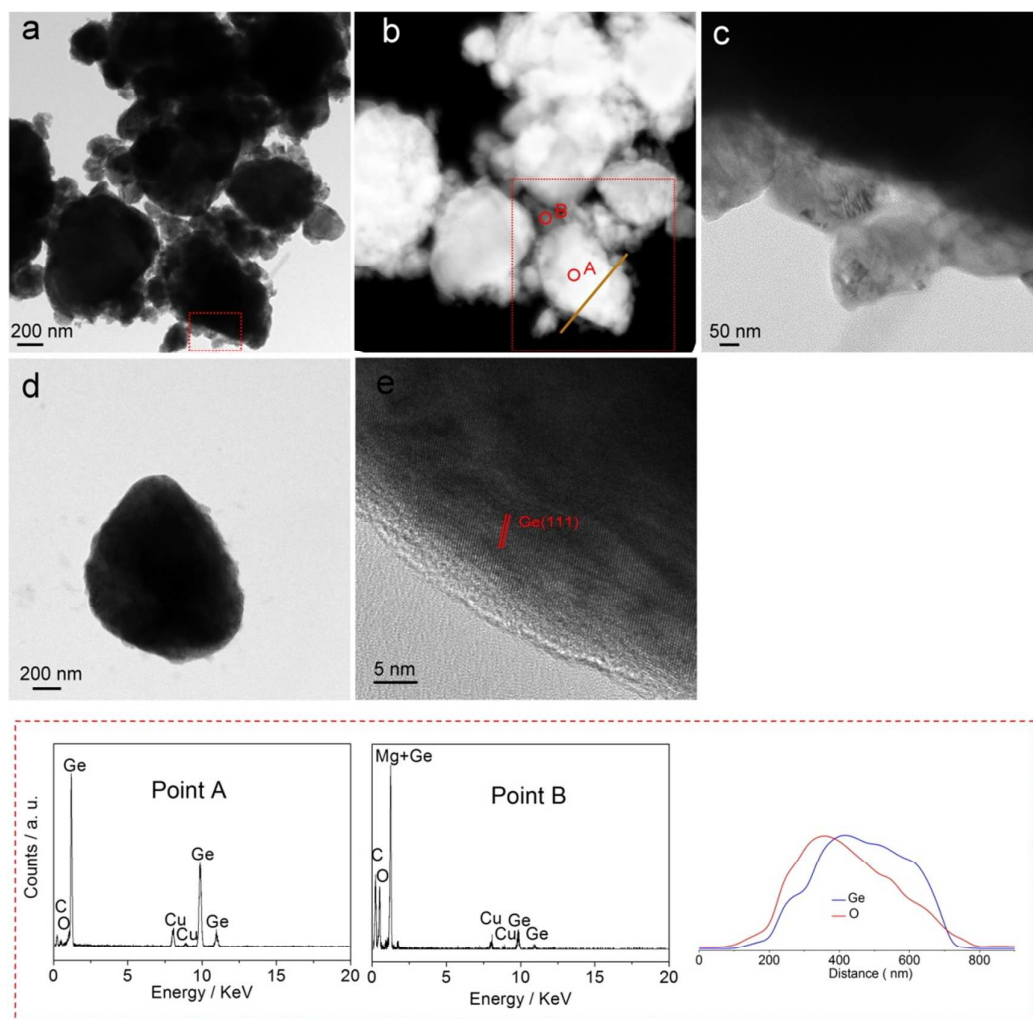


Fig.S4. Morphologies of the initial catalyst Ge NPs/MgO and bare Ge. (a),(c) TEM and (b) STEM images of the initial Ge NPs/MgO after ball-milling. Selected EDX patterns and the elemental mapping in the red box reveal that the GeNPs were surrounded by MgO clusters. (d),(e) TEM images of bare Ge. After HCl washing, the MgO clusters around Ge NPs were clearly dissolved.

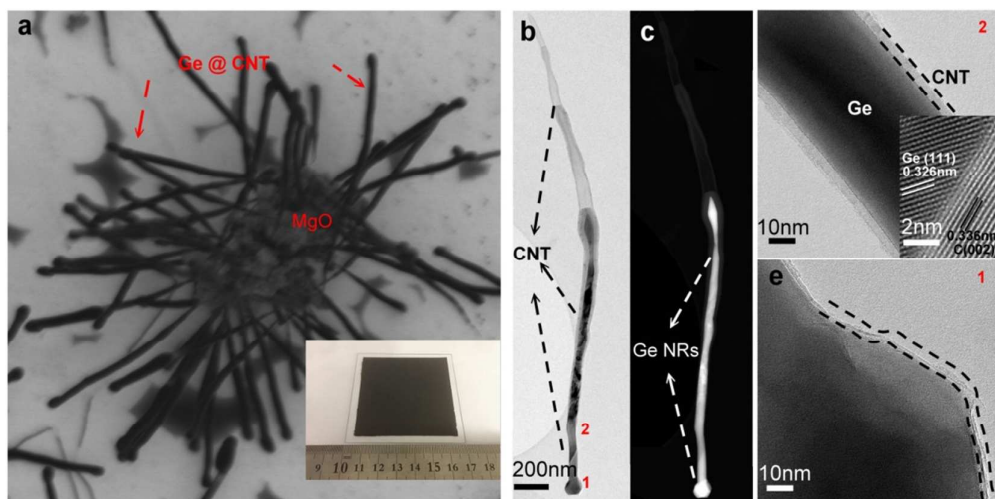


Fig.S5. Morphology of the Ge@CNT composite. (a) SEM images of the Ge@CNT composite with MgO clusters; (b),(d) and (e) TEM and (c) STEM images of the Ge@CNT composite; inset (d) high-resolution TEM image.

The morphology of the Ge@CNT composite was characterised by SEM and TEM. SEM images after CVD (Fig. S5 a) show that the Ge NPs were reshaped into nanorods inside CNT walls. A high yield of the core (Ge) plus shell (CNT) structure was obtained, as shown by the inset optical image in Fig.S5 a. TEM and STEM images of the core-shell structure (Fig.S5 b,c) reveal that Ge NRs are around 1.5  $\mu\text{m}$  long and are wrapped in carbon shells of thickness 5–10 nm (Fig.S5d). The (111) and (002) crystal plane fringes of the Ge NRs and CNTs were imaged by high resolution TEM (inset Fig.S5d). Note that the tip is covered by only 2–3 layers of carbon (Fig.S5 e); this permits diffusion of ions during (de)alloying without direct exposure of the Ge NRs to the electrolyte

#### 4. Electrochemical study of Ge@CNT and bare Ge

##### 4.1 Cyclic voltammograms (CVs) of Ge@CNT and bare Ge.

Fig.S6 shows the typical cyclic voltammograms (CVs) of Ge@CNT and bare Ge in the initial 6 cycles at a scan rate of 0.1 mV/s between 0.005-1V vs. Li/Li<sup>+</sup>. As shown in Fig.S6a, during the first reduction scan of Ge@CNT, the broad cathodic peaks below 0.7V are ascribed to both reduction of Ge and the decomposition of the electrolyte to form solid-electrolyte interface (SEI) corresponding to the capacity loss during the first cycle. This peak disappears during subsequent cycles while new well-defined peaks appeared. By the 4<sup>th</sup> reduction scan, voltammograms are stable and present four peaks, which are consistent with previous reports<sup>4,5</sup>. In the oxidation sweeps, narrow Li<sup>+</sup> oxidation peaks are assigned to the delithiation of Li<sub>x</sub>Ge. The increase in the oxidation peak height after the first cycle indicates improvement in Li ion extraction kinetics<sup>5</sup>. All peaks are reproducible and stable after first scanning, which reflect the reversibility of the electrochemical reaction of Ge@CNT electrodes. In contrast, the redox peaks of bare Ge decrease quickly and almost decay completely after six sweeps (Fig.S6b).

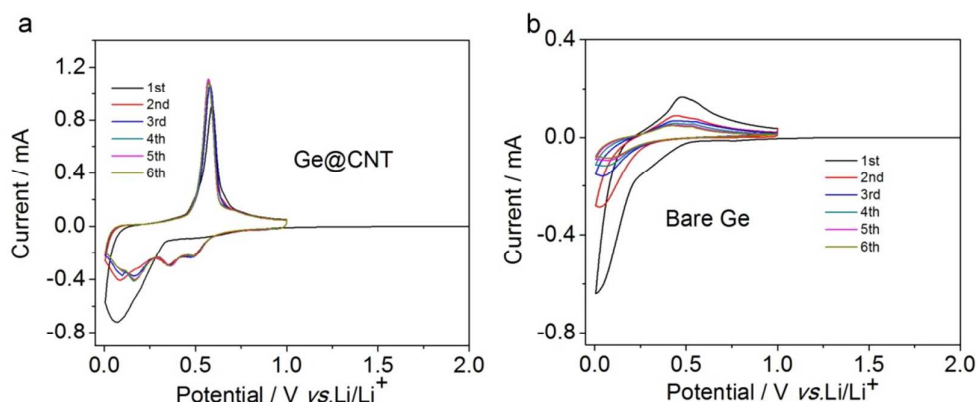


Fig.S6. Cyclic voltammograms of (a) Ge@CNT and (b) bare Ge at the scan rate of 0.1 mV/s in voltage range of 0.005-1V vs. Li/Li<sup>+</sup>.

#### 4.2 Voltage profiles of Ge@CNT at 0.2C

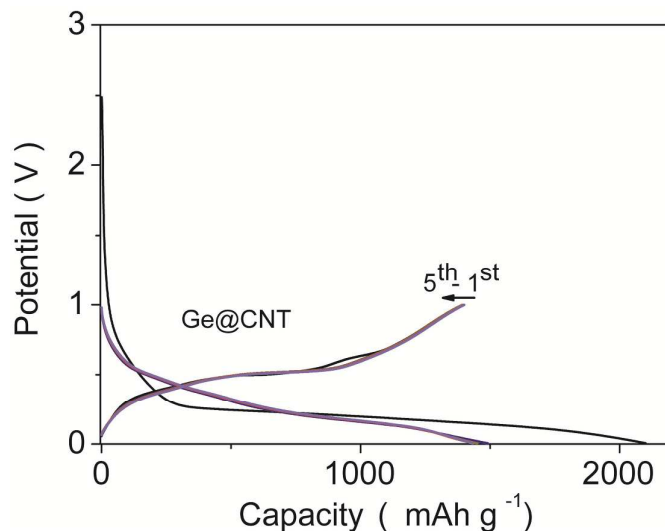


Fig.S7. First-five-cycles voltage plots of the Ge@CNT composite at 0.2C (1C = 1.6 A g<sup>-1</sup>).

Fig.S7 shows the first-five-cycle voltage profiles of Ge@CNT in the voltage range of 0.005–1 V vs. Li/Li<sup>+</sup> (all of the potentials stated hereafter are with respect to Li/Li<sup>+</sup> unless otherwise stated). In the first cycle, the specific lithiation and delithiation capacities of the Ge@CNT composite were 2100 mAh g<sup>-1</sup> and 1400 mAh g<sup>-1</sup> at 0.2C, respectively (1C = 1.6 A g<sup>-1</sup>; the coulombic efficiency was 67% in the voltage window of 0.005–1 V.) The initial irreversible capacity loss was due to the formation of passive solid electrolyte interface (SEI) layers and/or irreversible lithium insertion.<sup>6,7</sup> There was no obvious fading in charging capacity at the end of five cycles.



### 4.3 Rate capability of Ge@CNT and bare Ge

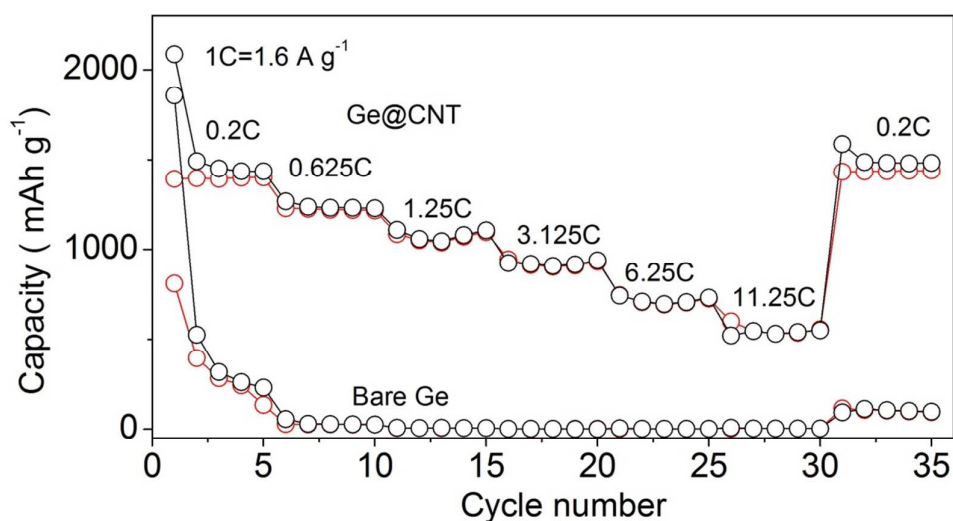


Fig.S8. Symmetric rate capability study of the Ge@CNT composite and bare Ge in the voltage range 0.005-1 V vs. Li/Li<sup>+</sup>;

The electrochemical performance of the Ge@CNT composite was evaluated using Li half-cells (2016R type). Working electrodes with a loading mass of  $\sim 1.5 \text{ mg cm}^{-2}$  were prepared by mixing Super P carbon black and polyvinylidene fluoride (PVDF) binder with the Ge@CNT composite in *N*-methyl-2-pyrrolidone (NMP) to form a slurry. The slurry was then coated onto copper foil and dried under vacuum overnight. The components comprised 85% Ge@CNT NRs, 5% Super P carbon black (5% MWCNT had already been grown in the composite) and 10 wt% PVDF binder. Using lithium foil as the counter-electrodes, the cells were cycled between 0.005 V and 1 V. As shown in Fig.S8, the Ge@CNT possesses a good rate capability. Even under a high discharge and charge rate of 11.25C (symmetric rate study: the same current densities were applied for discharge and charge), as shown in Fig.S8b, the Ge@CNT composite continued to exhibit a specific capacity of  $550 \text{ mAh g}^{-1}$ , 1.5 times higher than the theoretical capacity of graphite ( $372 \text{ mAh g}^{-1}$ ). Importantly, after the high-rate measurement, the specific capacity of the Ge@CNT composite cycled at under 0.2C was able to recover to the initial reversible values, indicating the robustness and stability of the Ge@CNT composite as an anode material.

#### 4.4 Asymmetric rate study (fast-discharge and slow-charge) of Ge@CNT

An asymmetric rate study (fast discharge and slow charge; see Fig.S9b, for the program) was also performed to evaluate the performance of the Ge@CNT composite in conditions of extreme discharging<sup>8,9</sup>. As shown in Fig.S9a, charging capacities of 595 mAh g<sup>-1</sup>, 500 mAh g<sup>-1</sup> and 274 mAh g<sup>-1</sup> were obtained at a charging rate of 0.2C, even at discharging rates of 62.5C, 75C and 93.75C, respectively (1C = 1.6 A g<sup>-1</sup> in the voltage window of 0.005–3V)<sup>10,11</sup>. This extreme electrochemical behaviour can be repeated without damaging the battery, as shown in Fig.S9b.

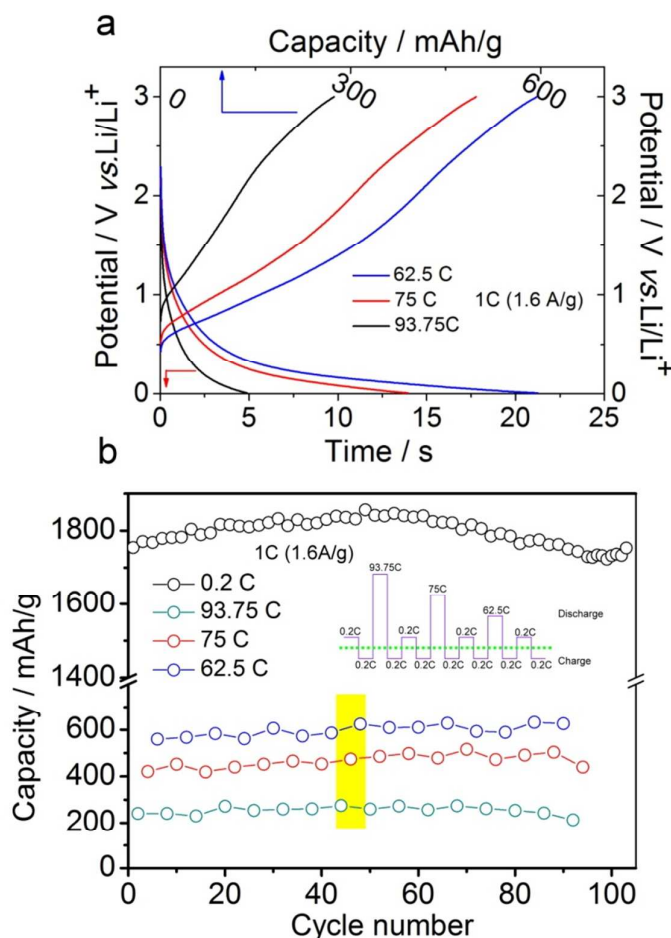


Fig.S9. (a) asymmetric rate capability study of the Ge@CNT composite in the voltage range 0.005–3 V vs. Li/Li<sup>+</sup> (second timescale discharge); (b) Cycling stability of Ge@CNT under asymmetric rate study in the voltage window of 0.005-3V vs. Li/Li<sup>+</sup>. Description of the program was inserted in the figure.

#### 4.5 Cyclability and Voltage profiles of Ge@CNT.

Fig.S10, S11 shows the cyclability and voltage profiles of Ge@CNT between 0.005-1V vs.  $\text{Li/Li}^+$  at 0.625C (a), 1C (b) and 1.875C(c) (the half-cell was lithiation/delithiation at 0.2C for the first cycle to form a smooth SEI). The highly stable and reversible capacity of 1216 mAh/g (charge capacity) is achieved for 100 cycles at 0.625C. At 1C, after 100 cycles, the retained capacity is 1124mAh/g. More importantly, the specific charging capacity after 200 cycles at 1.875 C is 975mAh/g with capacity retention of 92%. In contrast, bare Ge exhibits much lower specific capacity (140 mAh/g) after 100 cycles at 0.625C. The voltage window is 0.005-1V vs.  $\text{Li/Li}^+$ .

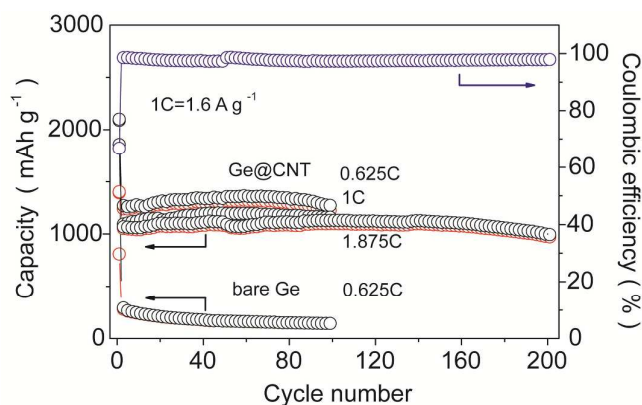


Fig.S10. Long-term stability of the Ge@CNT composite in the voltage range 0.005-1 V vs.  $\text{Li/Li}^+$ .

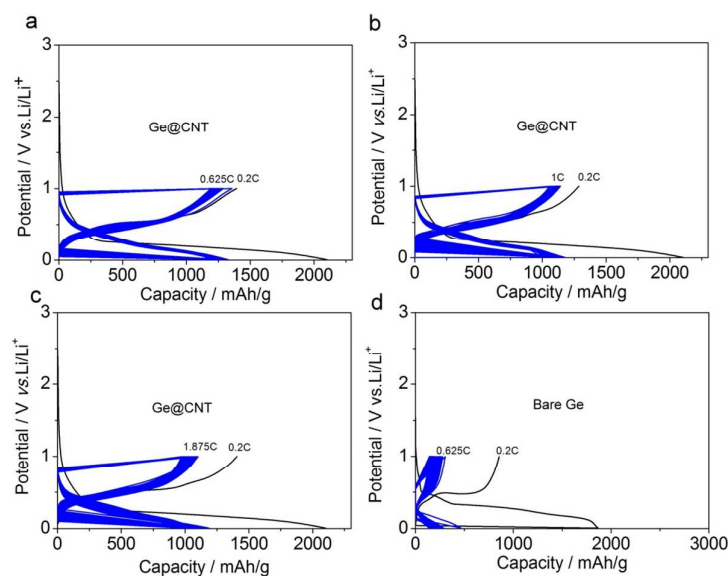


Fig.S11. Voltage profiles of Ge@CNT at (a)0.625C,(b)1C,(c)1.875C and (d)bare Ge at 0.625C between 0.005-1V vs.  $\text{Li/Li}^+$ .

#### 4.6 Ex-situ impedance study of Ge@CNT and bare Ge

Fig.S12a displays the impedance spectra of Ge@CNT and bare Ge before cycling. The superior rate capability of Ge@CNT should be attributed to the enhanced electrical conductivity. Importantly, as shown in Fig.S12b, even after 100 cycles, the lower inner resistance of Ge@CNT can be maintained very well, attesting to the long-term stability of Ge@CNT.

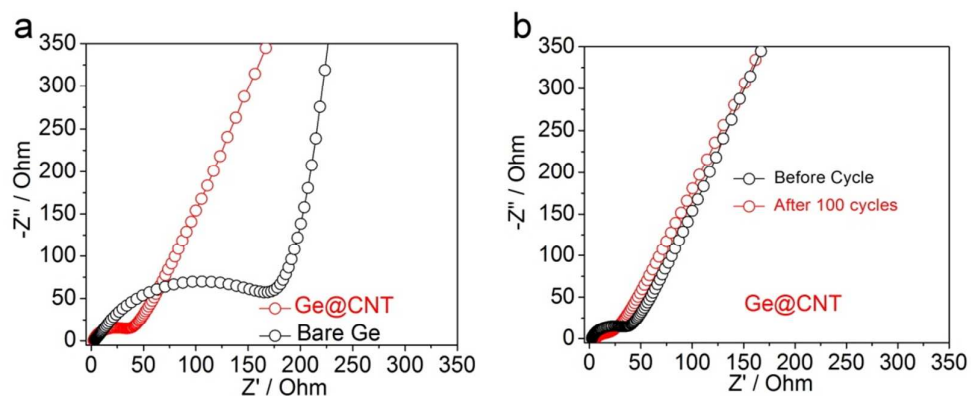


Fig.S12. Nyquist plots of bare Ge and Ge@CNT (a) before cycle and (b) after 100 cycles.

#### 4.7 Performance comparison of Ge@CNT and reported Ge-based anodes

Table S1. Performances of Ge-based anodes

Materials	Maximum reversible Capacity (delithiation; mAh/g(rate))	Cycle life at various rates cycle number (capacity retention) rate	Operation window / V vs. Li/Li <sup>+</sup>	Rate capability (mAh/g, delithiation(rate))	Mass loading	Weight ratio of active mass in the electrodes (the composite)	Carbon content (wt%) in the composite
Ge Nano wire <sup>12</sup>	1141(0.05C)	20(88%) 0.05C	~0-2.5	600 (2C)	~1 mg/pcs	100%	Nil.
Germanium–Carbon <sup>13</sup>	923(0.1C) 1C=1.6A/g	50(77%) at 0.1C then cycle at 0.187C, 0.375C and 0.562C for 50cycles respectively	0.05-1	650(0.375C) 613(0.562C)	Nil.	80%	58
Germanium/Carbon Nanostructures <sup>14</sup>	1184(0.2C) 1C=1.6A/g	120(74%) 1C <sub>1</sub> 80(50%) 20C <sub>1,2</sub> 100(40%) 40C <sub>1,2</sub>	0.01-1.5	1077(20C) <sub>1</sub> 480(40C) <sub>1</sub>	1 mg/cm <sup>2</sup> 1g/ml	80%	10-20
3D Porous Germanium <sup>15</sup>	1428(0.5C) 1C=1.6A/g	100(95%) 1C	0-1.2	1415(1C)	Nil.	80%	6
Germanium Porous Network(Tin seeded) <sup>16</sup>	1103(0.5C)	1100(80%)0.5C 200(80.2%)1C 80(92.6%)20C <sub>1</sub>	0.01-1.5	202(20C) 354(100C) <sub>1</sub>	0.22mg/cm <sup>2</sup>	100%	Nil.
Ge/Ti Nanomembranes <sup>17</sup>	1490(0.06C) 1C=1.6A/g	100(62%) 0.06C	0.05-1.5	930(0.06C) <sub>3</sub> 565(0.5C) <sub>3</sub>	Nil.	70%	Nil.
GeO <sub>2</sub> /Ge/C Nanocomposite <sup>18</sup>	1872(0.05C) 1C=2.1 A/g	50(93%)1C <sub>1,2</sub>	0.01-3	1750(5C) <sub>4</sub> 1680(10C) <sub>4</sub>	0.55mg/cm <sup>2</sup> 0.8g/ml	70%	23

Ge nanowire sheathed with carbon <sup>19</sup>	963 (0.5C) 1C=0.8A/g	100 (72%)0.5C	0-1.5	764(4C) <sub>4</sub> 700(6C) <sub>4</sub>	6 mg/cm <sup>2</sup>	80%	10
Ge/C Nanowires <sup>20</sup>	1428(0.2C) <sub>6</sub> 1C=1.6A/g	50(84%)0.2C 500(80%)10C	0.01-1.5	792(10C) <sub>5</sub> 690(20C) <sub>5</sub>	Nil.	85%	~4.3
Ge inverse opal with porous wall <sup>21</sup>	1276(0.2C)	100(88.9%)0.2C	0.01-2	~829(5C)	Nil.	100%	Nil.
Graphene/Ge Nanowire <sup>4</sup>	1350(0.05C) 1C=1.2A/g	400(92%)0.5C <sub>2</sub> 200(90%)4C <sub>2</sub>	0.001-1.5	800(10C) 363(20C)	1-1.9 mg/cm <sup>2</sup>	70%	1.7
Ge assembled on CNT <sup>22</sup>	1140(0.5C) 1C=1.6A/g	200(90%) 1C	0-1.2	620(3C) 490(5C)	Nil.	100%	35-40
Ge particle embedded in CNT <sup>23</sup>	750(0.045C) 1C=1.6A/g	20(107%) 0.045C	0.05-1	281(2.32C) 122(4.65C)	Nil.	80%	33
Ge@C /rGO <sup>6</sup>	1000(0.03C) 1C=1.6A/g	50(94%) 0.03C	0-1	380(2.25C)	Nil.	85%	38
Ge/RGO/C nanocomposites <sup>24</sup>	1166 (0.2C)	600(~100%)1C	0.01-1.5	720(20C) <sub>7</sub> 453(12C) 750(9.6C) <sub>8</sub>	0.6mg/cm <sup>2</sup>	75%	19.88
Ge@CNF <sup>25</sup>	883(0.15C) 1C=1.6A/g	100(84%)0.15C 250(~66%)1C	0.005-1.2	475(15C) 272(25C)	1mg/pcs	100%	51.9
This work	1401(0.2C) 1C=1.6A/g	100(97.8%) 0.625C <sub>2</sub> 200(92%) 1.875C <sub>2</sub>	0.005-1	550(11.25C) 274(93.75C) <sub>9</sub>	1.5 mg/cm <sup>2</sup>	85%	5

Footnote: 1. Lithiation at 0.5C; 2. Pre-activation at lower rate before cycle; 3. Tested after 100 cycles; 4.Lithiation at 0.1C; 5. The specific capacity calculated based on the mass of pure Ge; 6. Full cell was demonstrated; 7. Lithiation at 1.2C; 8. Tested at 55°C;9. Delithiation at 0.2C.

## 5. TEM study of phase evolution using TEM-coin cell configuration.

### 5.1 Physical integrity of the Ge@CNT composite after being discharged to 0.17 V and charged to 0.5 V at 0.2C.

Similar to a previous paper which reported the direct visualization of phase conversion in a high performance NiO anode material,<sup>26</sup> we applied the same method to observe the phase evolution of Ge and CNT during first lithiation/delithiation.

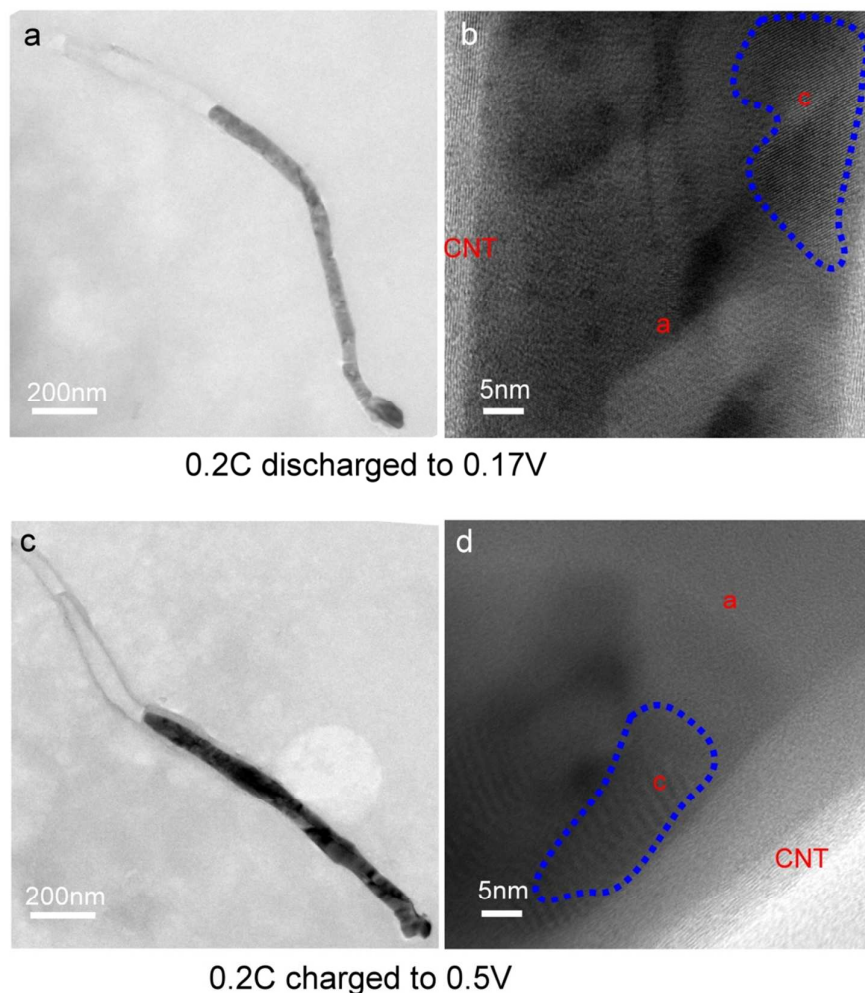


Fig.S13. TEM images of Ge @ CNT first (a),(b)discharged to 0.17V and (c),(d)charged to 0.5V at 0.2C.

The morphologies of Ge@CNTs composite which have been discharged to 0.17V and charged to 0.5V are preserved well. In the TEM images, it is observed that most of the Ge NRs is amorphous with crystalline domains embedded in. These results agree with the ex-situ XRD observations. We observed no obvious fracture of CNTs after delithiation, which ensures good electron transport during cycling.

## 5.2 TEM images of Ge@CNT after 200cycles

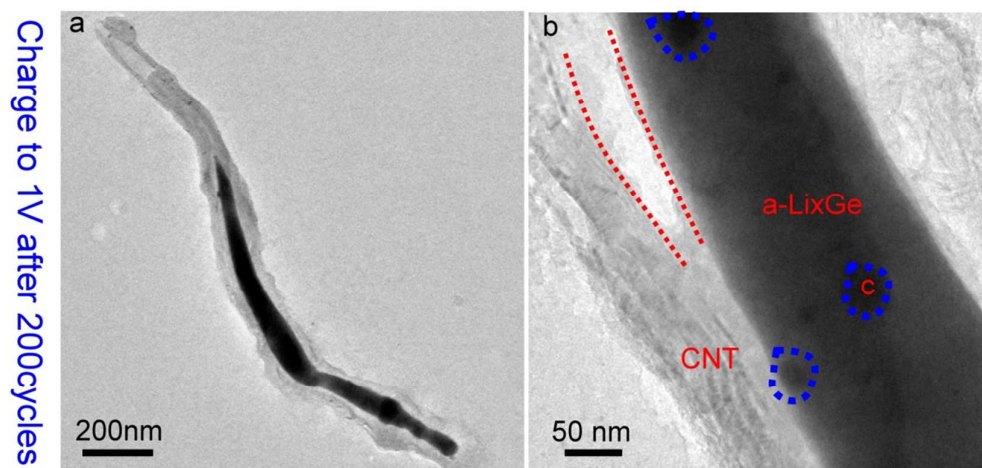


Fig.S14. TEM images of Ge@CNT charged to 1V after 200 cycles.

After 200 cycles at 1.875C by using the TEM-coin cell configuration, the morphology of Ge@CNT remains stable. With an amorphous property, Ge NRs are loosely packed in CNT walls with seeds of crystalline islands interspersed within. Such seeds are also found at first full delithiation. We believe the crystalline islands act as nuclei for the formation of a-Ge from c-Li<sub>15</sub>Ge<sub>4</sub> (or over-lithiated phase c-Li<sub>15+ $\theta$</sub> Ge<sub>4</sub>).



## 6. In-situ NMR configuration.

### 6.1 The illustration of the NMR measurement cell.

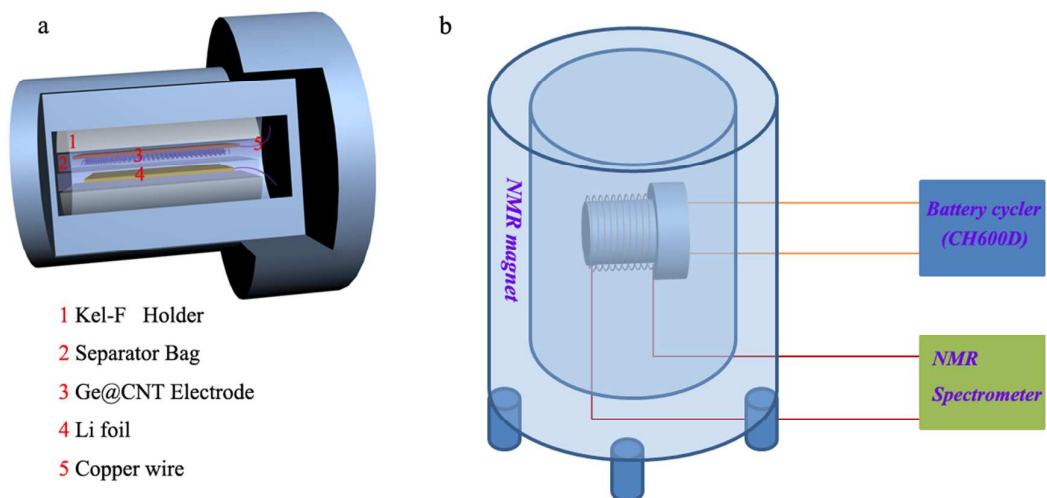


Fig.S15. Illustration of the (a) in-situ NMR battery holder and (b) in-situ NMR experiment design.

## 6.2 Fitting method for NMR data.

The peaks in the in-situ  $^7\text{Li}$  NMR spectra were deconvoluted using commercially available software, i.e., NUTs (v.2012, Acorn NMR Inc., Las Positas, CA, USA), where a mixed Gaussian and Lorentzian lineshape function can be easily implemented. Both the line-shape and the line-width for each peak are fixed, with variation of less than 5%, during the fitting of the entire spectral series as a function of the discharge-charge time. (i) The -24 ppm is well separated from the rest of the peaks for a good part of the discharge-charge potential range and its peak center and linewidth/lineshape can be uniquely determined and then fixed during the entire spectral series; (ii) The +24 ppm peak is also separated from the rest of the peaks at potentials of between 0.17 and 0.15 V, where the peak center and the lineshape/linewidth can be fixed and then used during the fitting of the entire spectral series; (iii) The Li-electrolyte and SEI signal (mainly the electrolyte signal) has three narrow peaks located at -3 ppm, -1 ppm and +4 ppm, respectively. Their linewidth and lineshape are uniquely determined as these signals are resolved and are significantly narrower compared to all other  $\text{Li}_x\text{Ge}$  signals. Mostly important, the signals from electrolytes and SEI are almost constant during the discharge-charge process; (iv) With -24, -3, -1, 4, 24 ppm peaks fixed, there is only one moving signal, i.e., the one with peak center changes from 13 ppm to 10 ppm gradually. This peak is needed in order to fit the spectral series and its peak center must be changed in order to generate the best fit. For example, at a discharge potential of 0.17 V during the first cycle, the peak center for the 24 ppm peak can be resolved from the rest of the peaks. The determination of the 13 and 10 ppm peaks are not straightforward and are determined by fitting the whole spectral region between -40 and +40 ppm.

### 6.3 Quantitative analysis of the phase compositions.

The relevant quantitative analysis about the phase distribution (based on NMR peak area) has been summarized in Table S2 following the methods of Eckert and Pöttgen, et al<sup>27,28</sup>.

Meanwhile, the cross-check of the phase distribution obtained from NMR and the total amount of lithium alloyed has been done. The phase distribution obtained from NMR matches well with the amount of lithium calculated from the electrochemical process at all the lithiation stages, except at the very ending of first discharge (0.005V, extra capacity around 90mAh g<sup>-1</sup> was obtained from the electrochemical process.). The extra capacity may have its origins in the surface functional group (-OH et al) on the composite, which will generate extra capacity at a deep discharge and as-grown defects of Ge<sup>29</sup>. This reaction is irreversible. We found that the phase distribution obtained from NMR matches well with the amount of lithium from the electrochemical process at the end of second discharge. The capacities of carbon lithiation and the initial formation of SEI passivation layers (345 mAh g<sup>-1</sup>) have been subtracted from the capacity in first discharge.

Table S2 Quantitative analysis of the phase compositions at the various stages during first two cycles

Potential /Capacity Discharge 1 <sup>st</sup>	1.18V / 0 mAh g <sup>-1</sup>	0.26 / 0	0.17 / 839	0.14 / 1086	0.11/ 1325	0.07/ 1459	0.005/ 1653
Phase index ( <sup>7</sup> Li chemical shift)	Component / Molar Ratio						
Li <sub>2.26</sub> Ge (24ppm)	-----	-----	1	0.413	-----	-----	-----
Li <sub>3.5</sub> Ge (13ppm)	-----	-----	-----	0.587	0.360	0.190-0.200	0.190-0.200
c-Li <sub>15</sub> Ge <sub>4</sub> (10ppm)	-----	-----	-----	-----	0.160	0.070-0.071	0.001-0.002
Li <sub>15+<math>\theta</math></sub> Ge <sub>4</sub> (-24ppm)	-----	-----	-----	-----	-----	0.141-0.145	0.200-0.215
Potential /Capacity Discharge 2 <sup>nd</sup>	1V/ 0 mAh g <sup>-1</sup>	0.40 / 244	0.25 / 604	0.15 / 934	0.10 / 1190	0.05 / 1357	0.005 / 1468
Phase index ( <sup>7</sup> Li chemical shift)	Component / Molar Ratio						
Li <sub>2.26</sub> Ge (24ppm)	-----	0.292*	0.724*	0.781	0.284	-----	-----
Li <sub>3.5</sub> Ge (13ppm)	-----	-----	-----	0.218	0.404	0.315-0.318	0.315-0.318
c-Li <sub>15</sub> Ge <sub>4</sub> (10ppm)	-----	-----	-----	-----	0.078	0.073-0.074	0.001-0.002
Li <sub>15+<math>\theta</math></sub> Ge <sub>4</sub> (-24ppm)	-----	-----	-----	-----	-----	0.095-0.099	0.174-0.178

\*There is no <sup>7</sup>Li NMR signal based on c-Ge or a-Ge. Thus Li<sub>2.26</sub>Ge is the only <sup>7</sup>Li NMR-detectable phase at these stages.

## 7. Experimental details.

**Growth of Ge@CNT:** Ge NPs/MgO catalyst was prepared through ball-milling magnesium (Mg) reduction of germanium dioxide ( $\text{GeO}_2$ ).  $\text{GeO}_2$  and Mg powders were received from Sigma-Aldrich without further treatment. The mixture of 1.0 g  $\text{GeO}_2$  and 0.6 g Mg powders were loaded and sealed under argon atmosphere into a 50 ml steel bowl containing 20 hardened steel balls in the diameter of 10 mm. After high-energy ball-milling of the mixture at a rotation rate of 450 rpm for 12 h on a planetary ball mill, the obtained composite was loaded on Alumina substrate and heated up to 880°C in 20 min in tube furnace, followed by CVD growth of Ge@CNT under a flow of hydrogen (50sccm) and methane (400sccm). Meanwhile, a side gas line was set up to bubble part of the mixture gas through a small water tank half-filled with distilled water (the flow rate was optimized as 8sccm). After 3h of growth, the samples were cooled to room temperature and washed by 50ml 1M HCl in flask under stirring for 30 min. After that, the Ge@CNT composites were collected by centrifuging and distilled water/ethanol washing. The alumina substrate can then be re-used for another round of growth. For comparison, bare Ge was prepared by direct washing away the MgO from the Ge NPs/MgO composite by HCl after ball-milling.

**Materials Characterizations:** Wide-angle X-ray diffraction (XRD) patterns were collected on Bruker D8 Focus Powder X-ray diffractometer using Cu K $\alpha$  radiation (40 kV, 40 mA). Scanning electron microscopy (SEM) analysis was performed on JEOL-6701F SEM. Transmission electron microscopy (TEM) analysis was performed on an FEI Titan 80-300 S/TEM (Scanning /Transmission Electron Microscope) operated at 200 kV. The elemental maps were obtained by the three-window method using Gatan Image Filter (GIF). Two pre-edge images were acquired for extrapolating the background which was then subtracted from the post-edge image to give elemental maps. Raman spectra were collected on Raman microscopy (Witech Alpha 300R, 532nm wavelength).

**Electrochemical measurement:** The electrochemical tests were performed using coin type 2016 half cell with lithium metal (Kyokuto Metal Co.,Ltd) as the counter and reference electrode and polypropylene film as a separator. The bare Ge electrodes were fabricated by mixing 80 wt% active materials, 10 wt% super p carbon black and 10 wt% PVDF binders while Ge@CNT electrodes were 85 wt% active materials, 5 wt% super p carbon black (5% MWCNT has already been grown in the composite) and 10 wt% PVDF binders in appropriate amount of NMP (N-methyl-2-pyrrolidinone, Sigma-Aldrich) as solvent. After stirring for 8 hours, the resulting paste was spread on a copper foil by Automatic Film Coater with Vacuum Pump & Micrometer Doctor Blade (MTI). After evaporation of NMP solvent in a vacuum oven at 120 °C for 12 h, the electrodes were pressed and cut into disks. The mass for each disk is around 1.5 mg/cm<sup>2</sup>. Cells were assembled in argon-filled glove box (MBraun, Germany,  $\text{O}_2 < 1\text{ppm}$ ,  $\text{H}_2\text{O} < 1\text{ppm}$ ). Cyclic voltammetry studies were carried on an IVIUMnSTAT multichannel electrochemical analyzer. The charge-discharge and cycling measurements were carried out using the Battery Test Stations (BitrodeCorp. St. Louis

Mo USA. Model: MCV 16-0.5/0.01-5) at room temperature about 23°C. Electrochemical impedance spectroscopy (EIS) was carried on cells using Autolab PGSTAT30 digital potentiostat/galvanostat at room temperature about 23°C. The frequency was varied from 0.1 MHz to 10 mHz with an alternating voltage signal amplitude of 10 mV.

**TEM-coin cell configuration:** For TEM-coin cell configuration, TEM grids loaded with Ge@CNT were pressed against normal anodic electrode (Ge@CNT loading on Cu foil). The TEM grid was then carefully removed and rinsed with DMC (dimethyl carbonate) in Argon-filled glove box ((MBraun, Germany,  $O_2 < 1\text{ ppm}$ ,  $H_2O < 1\text{ ppm}$ ) at the designated electrochemical stages, and directly transferred under Ar protection into TEM for characterization immediately. Noteworthy, we will not let the grid dry in the glove box to avoid unnecessary changes of samples. The pump in the loading cycle of our TEM can dry the grid very quickly (normally within 3 min) before characterization.

**Ex-situ XRD:** In order to understand the phase evolution of Ge@CNT electrodes during lithium cycles, ex-situ XRD experiments have been conducted. At different potential stages, electrodes were collected by disassembling the coin cells in Argon-filled glove box quickly. After rinsed in DMC (dimethyl carbonate), the electrodes were sealed in XRD holder by Mylar film (SPI Supplies, 2.5  $\mu\text{m}$ ) in Ar-filled glove box and sent to XRD characterization.

**NMR experiment:** The working electrodes were coated on copper foil with thickness of 9  $\mu\text{m}$ . The area density of Ge@CNT composite is little larger than the electrodes using in the coin cell study (around 2mg/cm<sup>2</sup>). Celgard 2500 separator (thickness of 25  $\mu\text{m}$ ) was made into the shape of a bag to hold the working electrode inside to isolate the Li metal electrode (thickness of 750  $\mu\text{m}$ ) and the working electrode. The battery cell was inserted into a specially designed in-situ NMR battery capsule case made of Kel-F, also named as PCTFE (PolyChloroTriFluoroEthylene) that can hold a planar battery with a tight seal of the battery components to prevent the exposure of the battery to air. The details of this new in situ battery holder will be published separately. The planar battery components were arranged such that the metal surface (both copper and Li-metal foil) is perpendicular to the external main magnetic field,  $B_0$ , and the direction of the excitation magnetic field,  $B_1$ , is parallel to both the copper and the Li-metal surface. A copper wire with diameter of 0.1 mm was linked to the copper foil of the Ge@CNT composite electrode via three needle holes at one end of the copper foil to create a good and secure electrical connection. A second copper wire of the same diameter was imbedded into the Li-metal electrode. Both wires were guided to the outside of the battery for charging and discharging of the in situ NMR battery *via* a CH600D instrument (Chronopotentiometry). The contents of the electrolytes were EC (Ethylene carbonate), DMC (dimethyl carbonate), DEC (diethyl carbonate) with volume ratios of 4:2:4, and 1 M LiFP<sub>6</sub>. The in situ battery was assembled in an argon-filled glove box by pre-drying the electrode components at 60 °C under vacuum in glove box chamber for 12 hours before assembling.

## Supplementary References

- (1) Hata, K.; Futaba, D. N.; Mizuno, K.; Namai, T.; Yumura, M.; Iijima, S. *Science* **2004**, *306*, 1362.
- (2) Zou, Y.; Wang, Y. *ACS Nano* **2011**, *5*, 8108.
- (3) Wang, Y.; Lee, J. Y. *Angew. Chem. Int. Ed.* **2006**, *45*, 7039.
- (4) Kim, H.; Son, Y.; Park, C.; Cho, J.; Choi, H. C. *Angew. Chem. Int. Ed.* **2013**, *52*, 5997.
- (5) Magasinski, A.; Dixon, P.; Hertzberg, B.; Kvit, A.; Ayala, J.; Yushin, G. *Nat. Mater.* **2010**, *9*, 353.
- (6) Xue, D. J.; Xin, S.; Yan, Y.; Jiang, K.-C.; Yin, Y.-X.; Guo, Y.-G.; Wan, L.-J. *J. Am. Chem. Soc.* **2012**, *134*, 2512.
- (7) Lee, H.; Kim, H.; Doo, S.-G.; Cho, J. *J. Electrochem. Soc.* **2007**, *154*, A343.
- (8) Ji, H.; Zhang, L.; Pettes, M. T.; Li, H.; Chen, S.; Shi, L.; Piner, R.; Ruoff, R. S. *Nano Lett.* **2012**, *12*, 2446.
- (9) Kang, B.; Ceder, G. *Nature* **2009**, *458*, 190.
- (10) Wang, Y.; Wang, Y.; Hosono, E.; Wang, K.; Zhou, H. *Angew. Chem. Int. Ed.* **2008**, *47*, 7461.
- (11) Zaghib, K.; Goodenough, J. B.; Mauger, A.; Julien, C. J. *Power Sources* **2009**, *194*, 1021.
- (12) Chan, C. K.; Zhang, X. F.; Cui, Y. *Nano Lett.* **2007**, *8*, 307.
- (13) Cui, G.; Gu, L.; Zhi, L.; Kaskhedikar, N.; van Aken, P. A.; Müllen, K.; Maier, J. *Adv. Mater.* **2008**, *20*, 3079.
- (14) Seng, K. H.; Park, M.-H.; Guo, Z. P.; Liu, H. K.; Cho, J. *Angew. Chem. Int. Ed.* **2012**, *51*, 5.
- (15) Park, M.; Kim, K.; Kim, J.; Cho, J. *Adv. Mater.* **2010**, *22*, 415.
- (16) Kennedy, T.; Mullane, E.; Geaney, H.; Osiak, M.; O'Dwyer, C.; Ryan, K. M. *Nano Lett.* **2014**, *14*, 716.
- (17) Yan, C.; Xi, W.; Si, W.; Deng, J.; Schmidt, O. G. *Adv. Mater.* **2013**, *25*, 539.
- (18) Seng, K. H.; Park, M.-h.; Guo, Z. P.; Liu, H. K.; Cho, J. *Nano Lett.* **2013**, *13*, 1230.
- (19) Seo, M. H.; Park, M.; Lee, K. T.; Kim, K.; Kim, J.; Cho, J. *Energy Environ. Sci.* **2011**, *4*, 425.
- (20) Liu, J.; Song, K.; Zhu, C.; Chen, C.-C.; van Aken, P. A.; Maier, J.; Yu, Y. *ACS Nano* **2014**, *8*, 7051.
- (21) Song, T.; Jeon, Y.; Samal, M.; Han, H.; Park, H.; Ha, J.; Yi, D. K.; Choi, J.-M.; Chang, H.; Choi, Y.-M.; Paik, U. *Energy Environ. Sci.* **2012**, *5*, 9028.
- (22) Hwang, I. S.; Kim, J.-C.; Seo, S.-D.; Lee, S.; Lee, J.-H.; Kim, D.-W. *Chem. Commun.* **2012**, *48*, 7061.
- (23) Cui, G.; Gu, L.; Kaskhedikar, N.; van Aken, P. A.; Maier, J. *Electrochim. Acta* **2010**, *55*, 985.
- (24) Yuan, F.-W.; Tuan, H.-Y. *Chem. Mater.* **2014**, *26*, 2172.
- (25) Li, W.; Yang, Z.; Cheng, J.; Zhong, X.; Gu, L.; Yu, Y. *Nanoscale* **2014**, *6*, 4532.
- (26) Lin, F.; Nordlund, D.; Weng, T.-C.; Zhu, Y.; Ban, C.; Richards, R., M.; L.Xin, H. *Nat. Commun.* **2014**, *5*, 3358.
- (27) Cattaneo, A. S.; Dupke, S.; Schmitz, A.; Badillo, J. P.; Winter, M.; Wiggers, H.; Eckert, H. *Solid State Ionics* **2013**, *249–250*, 41.
- (28) Dinges, T.; Hoffmann, R.-D.; van Wüllen, L.; Henry, P.; Eckert, H.; Pöttgen, R. *J. Solid State Electrochem.* **2011**, *15*, 237.
- (29) Hu, Y.-Y.; Liu, Z.; Nam, K.-W.; Olaf, J. B.; Cheng, J.; Xiao, H.; Matthew, T. D.; Xiqian, Y.; Kamila, M. W.; Lin-Shu, D.; Karena, W. C.; Peter, J. C.; Xiao-Qing, Y.; Clare, P. G. *Nat. Mater.* **2013**, *12*, 1130.